PAPER

Check for updates

Synthesis and optoelectronic properties of a promising quaternary metal oxide light absorber CuBiW₂O₈†

Lite Zhou,‡[ab] Edan Bainglass, [ID] ‡[c] Maryam Masroor,[ab] Binod Giri, [ID] [ab] Guangjiang Li, [ID] [d] Alexander Carl,[e] Ronald L. Grimm,[e] Muhammad N. Huda, [ID] [c] Lyubov V. Titova[d] and Pratap M. Rao [ID] ⋆[ab]

We have previously predicted CuBiW₂O₈ (CBTO) as a novel quaternary metal oxide semiconductor with favorable band gap for applications in photocatalysis and photovoltaics. Here, we report the synthesis of CBTO and the first characterization of its optical, electrical and photoelectrical properties. We demonstrate a Cu-rich solid state synthesis method that enables the synthesis of CBTO powders and continuous thin films. The CBTO contains bulk Bi₂WO₆ impurity that is not removed by annealing at higher temperatures, as well as CuO surface impurity. Density Functional Theory (DFT) calculations show that Bi₂WO₆ co-exists with CBTO due to reasons of thermodynamic stability and has a type II band offset that may result in electron trapping. CBTO is measured to have a direct band gap of ~1.9–2.0 eV (which is smaller than existing oxides Cu₂O and BiVO₄), and optical absorption coefficient of 10^4 to 10^5 cm^{-1} for visible-wavelength photons. DFT calculations match these results and show that Cu-vacancies are responsible for p-type conductivity, which was also measured by Hall effect. In addition, Hall effect, time-resolved photoluminescence (TRPL), and optical pump − THz probe spectroscopy (OPTP) measurements reveal that both slow hopping transport of trapped carriers (with 0.32 cm² V^{-1} s^{-1} mobility) over nanosecond timescales and fast band-like motion of free carriers (with ~150 cm² V^{-1} s^{-1} mobility) over picosecond timescales result in comparable diffusion lengths of ~10 nm. However, because this carrier diffusion length is shorter than the optical absorption depth (100–200 nm), nanostructured heterojunctions will likely be needed to achieve efficient solar energy conversion.

ᵃDepartment of Mechanical Engineering, Worcester Polytechnic Institute, Worcester, Massachusetts, 01609, USA. E-mail: pmrao@wpi.edu
ᵇMaterials Science and Engineering Graduate Program, Worcester Polytechnic Institute, Worcester, Massachusetts, 01609, USA
ᶜDepartment of Physics, University of Texas at Arlington, Arlington, Texas, 76019, USA
ᵈDepartment of Physics, Worcester Polytechnic Institute, Worcester, Massachusetts, 01609, United States
ᵉDepartment of Chemistry and Biochemistry, Worcester Polytechnic Institute, Worcester, Massachusetts, 01609, USA

† Electronic supplementary information (ESI) available: Methods of theoretical calculations, and supporting experimental and theoretical results, including optical and SEM images of the pelletized powders; XRD PDF standard patterns; EDS measurements of powders annealed with and without Cu-rich conditions; XRD patterns of powders annealed at higher temperatures; calculated thermodynamic chemical potential landscape; XPS spectra and accompanying discussion; expanded XRD patterns in the range of primary CuO and Cu₂O peaks; EDS measurements of rounded and plate-like particles in powders annealed under Cu-rich conditions; direct gap Tauc plot; band offsets of CBTO and Bi₂WO₆; UPS spectra; and XRD patterns and SEM images of powders sintered into continuous films on quartz and ITO substrates. See DOI: 10.1039/d0ta07653h

‡ Equal contributions.

1. Introduction

Metal oxide semiconductors are promising candidates as light absorbers in photocatalysis and photovoltaics. As thin films, many metal oxides could offer earth-abundant, non-toxic alternatives to other thin-film materials such as CIGS and CdTe, allowing us to tap our plentiful solar energy resource more cost-effectively and at a larger scale than is possible with today's materials.[1–7] However, metal oxides usually have large band gaps or poor charge transport properties, or both. Efficient carrier photoexcitation and transport are mutually exclusive in most of the binary metal oxides: those with good charge transport properties such as ZnO,[8,9] SnO₂,[10,11] and WO₃ (ref. 12 and 13) suffer from large band gaps (≥2.7 eV) which prevent efficient light absorption, while others such as Fe₂O₃,[14,15] and Co₃O₄ (ref. 16) have moderate band gaps (0.9–2.2 eV) but are extremely poor at transporting carriers. Poor transport of photoexcited charges in oxides can result from low carrier mobility, low photoexcited carrier lifetime, or both. Low mobility can be due to hopping-type or polaron-type transport mechanism in oxides as a result of the ionic character of the crystal, and/or due to scattering at defects. Low lifetime can be

This journal is © The Royal Society of Chemistry 2021

J. Mater. Chem. A, 2021, **9**, 1643–1654 | **1643**

due to fast direct recombination across a direct band gap and/or due to recombination at defects. In addition, both low mobility and low lifetimes can be due to high or uncontrolled majority carrier concentration as a result of high defect concentration.

With good charge transport properties and a moderate band gap, Cu_2O-based PV cells recently achieved the highest solar conversion efficiency (8.1%)[3] among all metal oxides. However, the relatively large band gap of Cu_2O (~2.2 eV) still prevents it from absorbing the yellow, orange and red portions of the solar spectrum, which limits the solar energy conversion efficiency. Doping binary metal oxides with other metals (at relatively low concentrations, without changing the parent crystal structure) to improve optoelectronic properties has been extensively investigated, but charge transport properties have not been improved and improvements in band gap are modest.[17–20] A natural direction for simultaneously achieving moderate band gaps and good charge transport properties is alloying to obtain multi-metal oxides. This is distinct from doping in that the multi-metal oxides form entirely new crystal phases with distinct properties from the constituent oxides.

In this paper, for the first time, we report the synthesis and characterization of a theoretically-predicted quaternary metal oxide phase, $CuBiW_2O_8$ (CBTO). CBTO powders were synthesized by a Cu-rich solid-state synthesis method, in which fine Bi_2O_3, Cu_2O, WO_3 powders were mixed and repeatedly annealed in a Cu-rich atmosphere. As device applications require continuous conduction paths for long-range charge carrier transport, we have also developed approaches to synthesizing CBTO pellets and continuous CBTO films on ITO and quartz substrates. The bulk composition, crystallinity and morphology of the resulting CBTO materials were studied by X-ray diffraction (XRD), scanning electron microscopy (SEM), and energy dispersive X-ray spectroscopy (EDS), while the surface composition was studied by X-ray photoelectron spectroscopy (XPS). The optical absorption and band gap were measured by UV-vis absorbance and steady-state photoluminescence (PL), while the surface electronic structure was measured by ultraviolet photoelectron spectroscopy (UPS). The concentration and mobility of carriers was measured by Hall effect, while the lifetime of photoexcited carriers was measured over nanosecond timescales by time-resolved photoluminescence spectroscopy (TRPL). Finally, the lifetime and mobility of free photoexcited carriers within and across individual grains was measured over picosecond timescales by optical pump-terahertz (THz) probe spectroscopy (OPTP). These measurements collectively show that this approach yields CBTO that contains Bi_2WO_6 bulk impurity that appears to co-exist with CBTO at thermodynamic equilibrium (which is also verified by density function theory calculations of thermodynamic stability), as well as CuO surface impurity. In addition, the measurements show that the synthesized quaternary CBTO has strong optical absorption across the visible range and promising values for mobility of photoexcited carriers compared to ternary metal oxides $BiVO_4$ and $CuBi_2O_4$. To the best of our knowledge, this is the first time that the optical, electrical and photoelectrical properties of CBTO have been studied.

2. Background

Ternary metal oxides ($A_xB_yO_z$) in which A is a ns^2 metal cation (Bi^{3+}, Sn^{2+}, Sb^{3+}) and B is a md^0 metal cation (V^{5+}, Nb^{5+}, Ta^{5+}, Mo^{6+}, W^{6+}) are promising for solar energy conversion. They often have moderate band gaps due to hybridization of the ns^2 cation states with O 2p states, and relatively good charge transport properties due to the formation of large-polaron carriers by the hybridization of the md^0 cation states with O 2p states.[21] $BiVO_4$ is a typical ns^2–md^0 ternary metal oxide with 2.4 eV band gap. The moderate band gap along with relatively good charge transport properties have allowed $BiVO_4$ become one of the best-performing semiconductor photoanodes for photoelectrochemical water oxidation.[22] $BiVO_4$ is an n-type semiconductor in which photoexcited carriers have mobility of ~4×10^{-2} cm^2 V^{-1} s^{-1}, lifetime of ~40 ns, and resulting diffusion length of ~70 nm.[23] Another typical ns^2–md^0 ternary metal oxide, Bi_2WO_6 with 2.8 eV (ref. 24) band gap, also showed some potential in photocatalytic applications.[25,26] Recently, a promising ternary metal oxide light absorber $CuBi_2O_4$ was investigated. $CuBi_2O_4$ is a p-type semiconductor with band gap of ~1.8 eV, low carrier mobility of 1.2×10^{-3} cm^2 V^{-1} s^{-1} (due to heavy conduction band localization[27]), carrier life time of ~800 ns and carrier diffusion length of 52 nm.[28] It has been investigated as a photocathode for photoelectrochemical water splitting, and several efforts have been made to improve its charge separation efficiency.[29–31] Nonetheless, there is still a gap in terms of the discovery of metal oxide light absorbers that can achieve high efficiency by having carrier diffusion lengths comparable to the light absorption depth.

Meanwhile, we have theoretically predicted a new quaternary metal oxide $CuBiW_2O_8$ (CBTO) without any prior experimental knowledge as a promising semiconductor with strong optical absorption and a favorable band gap.[32] The bottom of the conduction band in CBTO is dominated by Bi 6p and W 5d orbitals, which is similar to the conduction band of Bi–W based oxides.[32,33] On the other hand, the band gap of CBTO is significantly reduced compared to BiW_2O_6 due to the presence of the Cu 3d orbital, which raises the top of the valence band in energy compared to that of Bi_2WO_6. Until now, no CBTO-based devices have been reported as CBTO synthesis presents many challenges such as maintaining Cu in Cu^{1+} rather than in Cu^{2+} oxidation state, suppressing the loss of volatile Cu, and contamination by the interdiffusion of Cu between substrates and CBTO at high growth temperatures.[34] The only report of CBTO synthesis appeared more than three decades ago and did not provide details on synthesis or optical, electrical, photoelectrical or structural characterization.[35]

3. Experimental section

Synthesis of CBTO powders was firstly attempted by a standard solid-state synthesis method in argon atmosphere. In this method, 0.466 g Bi_2O_3 (99.9%, Sigma Aldrich), 0.928 g WO_3 (99.9%, Sigma Aldrich) and 0.143 g Cu_2O (>99.99%, Sigma Aldrich) were mixed and ground in a glass vial by ball milling (500 rpm) for 20 hours. The mixed powders were then placed in

1644 | J. Mater. Chem. A, 2021, **9**, 1643–1654

This journal is © The Royal Society of Chemistry 2021

a ceramic boat and reacted by annealing in a tube furnace at 600 °C for 9 hours under 500 sccm flow rate of argon (99.995%, Praxair). This sample will be referred to as "annealed in Ar". The solid-state synthesis method was then modified by annealing mixed powders, as suggested by our first theory paper,[32] in a Cu-rich argon atmosphere. In the modified method, the same quantities of mixed and ball-milled powders were placed in a copper box constructed from Cu sheets (99.9%. Alfa Aesar). Then, the copper box was sealed by thin copper foil (99.99%. Alfa Aesar) to ensure that the powders were reacted in a nearly closed environment with Cu-rich atmosphere. The powders in the sealed copper box were then annealed and reacted in a tube furnace at the same condition. This sample will be referred to as "annealed 1 time in Cu-rich atmosphere". The powders annealed in Cu-rich atmosphere were then again ball-milled and annealed in Cu-rich atmosphere a second, third and fourth time (referred to as "annealed 2 times in Cu-rich atmosphere", "annealed 3 times in Cu-rich atmosphere", and "annealed 4 times in Cu-rich atmosphere"). The Cu-rich annealing was also carried out at temperatures of 700 and 800 °C for comparison. The phase composition and crystallinity of the powders were characterized by XRD (PANalytical Empyrean, Cu Kα, 45 kV, 40 mA). The morphology of the powders synthesized by annealing in Cu-rich atmosphere was characterized by scanning electron microscopy (SEM, JEOL 7000F, 5 kV). The samples for SEM, optical absorption, and steady-state PL measurements were prepared by firstly ball milling the powders for 20 hours. Then, the powders were dispersed in a mixed solvent including 14 mL 1-butanol (99.9%, Sigma Aldrich), 1 mL chloroform (99.5%, Sigma Aldrich) and 1 mL methanol (99.9%, Sigma Aldrich) to make a suspended solution. After 10 min sonication, the suspended solution was drop-casted onto a FTO/glass substrate (for SEM imaging) or onto a quartz substrate (for optical absorption, steady-state PL, and OPTP measurements). The samples for XPS, TRPL, Hall effect, and UPS measurements were prepared by pelletizing the powders that had been annealed 4 times in Cu-rich atmosphere by mechanically pressing them into a sealed Cu box. The powders were then annealed and sintered in a tube furnace at 600 °C for 9 hours with 500 sccm flow rate of argon to obtain a dense pellet. The optical image and the SEM images of the pellet are provided in ESI Fig. S1 and S2.† The pellet was 450 μm thick with 1 cm² area. Thin films of interconnected CBTO particles were synthesized on ITO/glass substrates for XRD and SEM analysis and on quartz substrates for OPTP measurements. For this, 4-times Cu-rich annealed powders were dispersed by sonication in a mixed solvent (as described above), filtered through 2 μm pore size filter papers and drop-casted onto the substrates, followed by annealing in sealed Cu boxes in a tube furnace at 500 °C for 9 hours with 500 sccm flow rate of argon to sinter the particles together.

4. Results and discussion

4a. Composition and morphology

The phase composition and crystallinity of the powders were characterized by XRD. The powder diffraction file (PDF)

standard patterns of the phases considered are shown in ESI Fig. S3.† The XRD patterns of the powders annealed 1 time in Ar without Cu-rich atmosphere, and annealed 1–4 times in Cu-rich atmosphere (all at 600 °C) are shown in Fig. 1. As seen from these patterns, the powders annealed in Ar without Cu-rich atmosphere are composed primarily of WO_3 and Bi_2WO_6, with small peaks from Bi_2O_3, $Bi_2W_2O_9$, and CuO. CBTO was not synthesized under this condition. Furthermore, energy dispersive X-ray spectroscopy (EDS) analysis shows that Cu is present in much lower quantity than expected (ESI Fig. S4 and Table S1†), indicating some loss of Cu during annealing. While the mechanism of Cu loss is not known, it could be due to evaporation of compounds containing Cu, or diffusion of Cu into the porcelain boat.[36] In the powders synthesized by reaction in the Cu-rich atmosphere, however, CBTO was successfully synthesized. The major phase is triclinic CBTO and the detectable impurity phases are orthorhombic Bi_2WO_6, orthorhombic $Bi_2W_2O_9$ and monoclinic WO_3. The XRD peaks for $Bi_2W_2O_9$ and WO_3 were no longer detectable when the powders were annealed 2, 3 and 4 times in the Cu-rich atmosphere. The XRD peaks for orthorhombic Bi_2WO_6 became successively weaker after 2 and 3 times annealing in Cu-rich atmosphere, which indicates that the amount of Bi_2WO_6 in the powders are significantly reduced by the Cu-rich annealing. However, the XRD pattern of 4 times Cu-rich annealed powders is almost identical to that of 3 times Cu-rich annealed powders, which indicates that Bi_2WO_6 cannot be completely removed by repeated Cu-rich annealing.

The Cu-rich annealing of the ball-milled powders was also performed 1 time at temperatures of 700 and 800 °C, to determine if faster kinetics or modified thermodynamics can enable the complete conversion to CBTO. XRD analysis (ESI Fig. S5†) shows that the amount of Bi_2WO_6 impurity increased with increasing annealing temperature. This indicates that
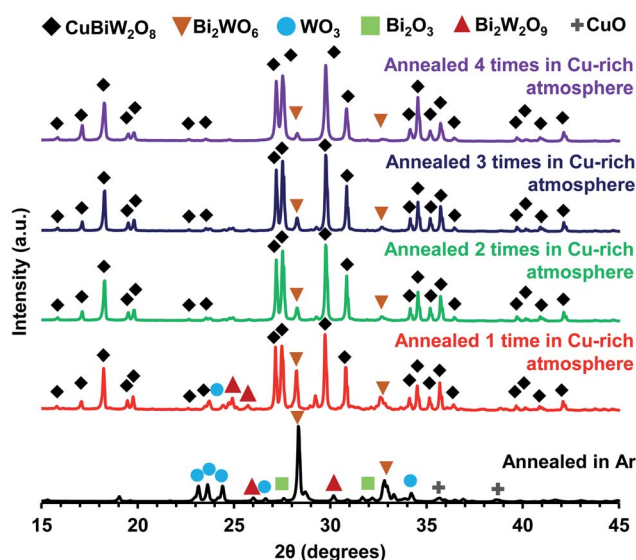

Fig. 1 X-ray diffraction of ball-milled powders annealed in Ar (without Cu-rich atmosphere) (black) or annealed 1 time (red), 2 times (green), 3 times (blue) or 4 times (purple) in Cu-rich atmosphere.

This journal is © The Royal Society of Chemistry 2021

J. Mater. Chem. A, 2021, **9**, 1643–1654 | **1645**

conversion of Bi_2WO_6 to CBTO ($Bi_2WO_6 + Cu_2O + 3WO_3 \leftrightarrow 2CuBiW_2O_8$) is not hindered by kinetics at these temperatures, but is rather controlled by thermodynamics. Based on this, Bi_2WO_6 co-exists with CBTO at thermodynamic equilibrium. The observation that the amount of Bi_2WO_6 impurity increases with temperature is consistent with a negative change in entropy for the forward reaction, which decreases the thermodynamic driving force (makes the free energy change less negative).

To further test for thermodynamic stability, we conducted a study of the chemical potential landscape[37] of CBTO and its stable fragments within the framework of density functional theory (DFT).[38] This approach allows prediction of a single-phase region, if one exists, within thermodynamic stability limits of a compound. Tuning synthesis conditions to within the bounds of the single-phase region ensures the purity of a product by enthalpically prohibiting the formation of its fragments. In general, the landscape of a quaternary metal oxide is 3-dimensional, with the value of the anion species derived from the values of the three axes using eqn S4a (see ESI†). However, as was done here, one can project the landscape onto several 2-dimensional planes using a variable chemical potential for a given species – Cu in the present case. To reflect both our earlier theoretical prediction, as well as the experimental setup mentioned above, Cu-rich conditions were considered, *i.e.* $\Delta\mu_{Cu} = 0$ eV. We provide computational details in ESI,† as well as similar additional analyses with respect to variations in Bi and W chemical potentials.

The chemical potential landscape of CBTO is presented in Fig. 2. The highlighted region, derived from eqn S4a–h,† represents one in which all but the bismuth tungstate (Bi_2WO_6) fragment of CBTO are thermodynamically unstable. This result is independent of the choice of the variable species (ESI Fig. S6†). We conclude that no single-phase region can exist for CBTO under thermodynamic consideration, and that Bi_2WO_6 is expected to persist as an impurity phase. This agrees with our

experimental findings, in which annealing the powders in a Cu-rich atmosphere did not completely eliminate the Bi_2WO_6 impurity. The presence of Bi_2WO_6 in CBTO appears to be a thermodynamic phenomenon.

A defect formation analysis[37] was conducted to study intrinsic point defect formations in CBTO, including vacancies and anti-sites. Conditions at the five corners of the region of interest (Fig. 2) were used in eqn S6b.† Further methodological details are given in ESI.† Results are shown in Fig. 3. Cu vacancies, or V_{Cu}, are constant at 0.348 eV due to the Cu-rich conditions, which suggests the likelihood of Cu vacancy
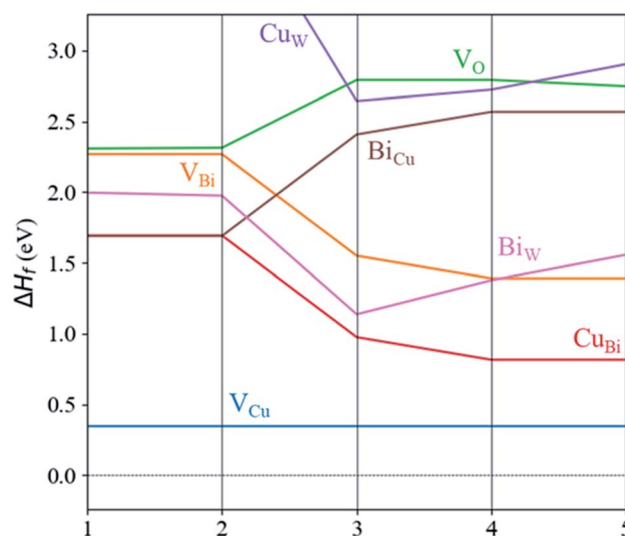

Fig. 3 Calculated defect formation enthalpies for vacancies and anti-sites in CBTO. Enthalpies are calculated at conditions bounding the region of interest (Fig. 2). Negative enthalpies indicate spontaneous formation. All values are calculated at 0 K. Thermal conditions during synthesis suggest a high probability of spontaneous Cu vacancy (V_{Cu}) formation.
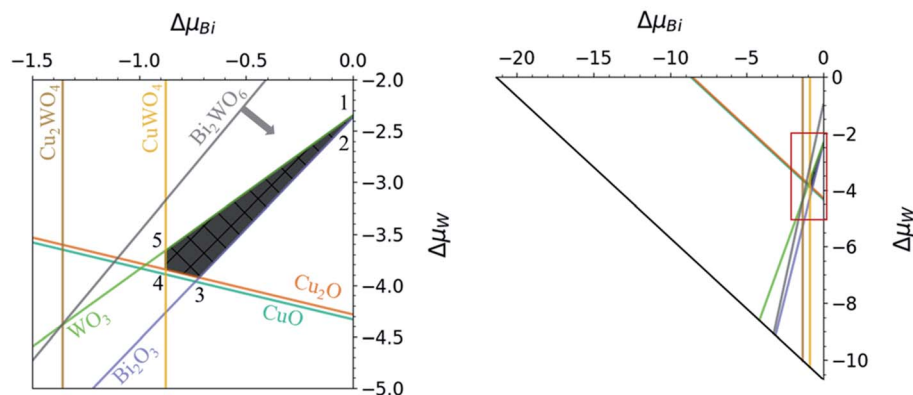

Fig. 2 Chemical potential landscape for $CuBiW_2O_8$ (CBTO) as a function of constituent chemical potentials (zoomed at left). Outer bounds represent the entire CBTO thermodynamic stability region (right triangle). Cu chemical potential ($\Delta\mu_{Cu}$) is set to zero reflecting experimental Cu-rich conditions. The bounding CBTO fragments Bi_2O_3, Cu_2O, and WO_3 correspond to the synthesis route taken experimentally. The shaded region contains points in which all CBTO fragments are thermodynamically unstable, except for Bi_2WO_6, which is thermodynamically stable in the direction indicated by the arrow (zoomed view). The numbered corners reflect chemical conditions used for defect formation calculations (Fig. 3). All Cu-containing compounds are calculated using DFT+U with $U_{eff} = 6$ eV on Cu 3d bands.

1646 | *J. Mater. Chem. A*, 2021, **9**, 1643–1654

This journal is © The Royal Society of Chemistry 2021

formation at synthesis temperatures. Cu-in-Bi anti-site, or Cu_{Bi}, dips in energy with decreasing Bi and W concentrations and may play a role depending on the concentration of Bi at synthesis. Bi_W behaves similarly, though a decrease in $\Delta\mu_W$ along the Cu_2O and $CuWO_4$ boundaries offsets increasing $\Delta\mu_{Bi}$ at lower Bi concentrations. Other defects remain relatively high in energy and are less likely to form. Overall, a high concentration of Bi and W during synthesis is determined to reduce the likelihood of defect formation, though further study of the effects of such defects on the properties of CBTO is warranted.

We then performed chemical characterization of the surface of the pelletized powders (that had been annealed 4 times in Cu-rich atmosphere and then pelletized by mechanical pressing and additional annealing under Cu-rich atmosphere) using XPS measurements, which are sensitive to the top few nanometers of the surface of the sample. Our XPS measurements and analysis (ESI Fig. S7† and accompanying analysis) clearly show the presence of both Cu^{1+}, as well as Cu^{2+} spectral features coming from the surface of the material, in addition to broadened Bi^{3+} and W^{6+} features. Cu^{1+} is the expected oxidation state of Cu in CBTO. However, the presence of Cu^{2+} indicates the presence of CuO or some other Cu^{2+} oxide on the surface. The Cu^{1+} features and broadened Bi^{3+} and W^{6+} features likely come from a combination of CBTO and Bi_2WO_6. Steady-state photoluminescence (PL) measurements that are presented later in the study show emission at ~1.4 eV, which matches the band gap of CuO. Therefore, we ascribe the Cu^{2+} signal coming from the surface of the material to CuO. The Cu^{1+} and Cu^{2+} spectral features have similar intensity and peak area, indicating a relatively large fraction of CuO at the surface. XPS with sputtering and depth profiling cannot be used in this case to determine whether the CuO is present only in a surface layer or distributed throughout the material because CuO (Cu^{2+}) is quickly reduced to Cu_2O (Cu^{1+}) by sputtering.[39]

From the above results, CuO was detected strongly by XPS (a surface-sensitive technique) and weakly by PL (a bulk technique that is weakly sensitive to the surface), but not by XRD (a bulk technique). To make it easier for the reader to see that Cu oxides (Cu_2O and CuO) are not detected by XRD, the XRD pattern for the 4-times Cu-rich annealed powders is plotted with an enlarged x-axis (2θ) scale in the range of angles in which these oxides have major peaks (ESI Fig. S8†). Indeed, the peaks in this range match closely with those of the CBTO standard rather than those of the CuO or Cu_2O standards, and not even small peaks are seen at the values expected for CuO or Cu_2O. Therefore, we can state that crystalline CuO or Cu_2O phases are not present down to the ~1% detection limit of XRD. However, since XRD only detects crystalline phases, one may still be concerned that some Cu oxide is present in amorphous form. However, according to literature reports, we can be reasonably sure that the sample does not contain amorphous Cu oxide impurities because the annealing temperature used here (600 °C) is much higher than the temperature needed to crystallize these oxides. For instance, annealing of solution-deposited Cu precursors at temperatures higher than 473 K (~200 °C) has been found to crystallize them into copper oxides, with crystallization becoming rapid at 623 K (350 °C).[40] Similarly, in the

case of thermal annealing of Cu films in air, it has been shown that the initial oxidation of the copper films starts at about 150 °C, a well ordered crystalline phase of Cu_2O is observed above 200 °C, a crystalline phase of CuO starts to appear at 320 °C, and a well ordered crystalline phase of CuO is observed at 350 °C.[41] In all these cases, these oxides synthesized by annealing at temperatures of ≤350 °C have strong, clearly identifiable XRD peaks. Therefore, we conclude that the material contains a surface layer with high CuO content (detected by XPS and PL), but that the total quantity of Cu oxide impurity (CuO or Cu_2O) is below the 1% detection limit of XRD. It is noted that a surface layer of CuO is also commonly reported on thermally-annealed Cu_2O films.[42] In addition, the material contains Bi_2WO_6 impurity both at the surface and in the bulk, detected by both XPS and XRD.

According to SEM images (Fig. 4), the powders obtained by annealing 1 time at 600 °C in Cu-rich atmosphere were composed of crystallites in the form of plates and rounded particles, while the only visible particle morphology in the powders obtained by annealing 4 times in Cu-rich conditions is rounded particles. We have performed EDS analysis on the rounded and plate-like particles from the powders annealed 1 time under Cu-rich atmosphere, as shown in ESI Fig. S9 and Table S2.† The atomic composition of the rounded particles closely resembles that of $CuBiW_2O_8$, with slightly higher Cu than expected, which could be due to the presence of surface impurity, consistent with the Cu^{2+} that was detected by XPS. The atomic composition of the plate-like particles shows firstly that they have little or no Cu, and that they are likely composed of some combination of Bi_2WO_6, $Bi_2W_2O_9$, Bi_2O_3, and WO_3. Bi_2WO_6, $Bi_2W_2O_9$ and WO_3 were indeed identified in the XRD pattern of 1-time Cu-rich annealed powder. According to previous reports on Bi_2WO_6, most crystalline Bi_2WO_6 particles indeed have plate or flake shapes.[26,43,44] Furthermore, the XRD result shows that $Bi_2W_2O_9$ seems to be eliminated by annealing 4 times under Cu-rich conditions, while Bi_2WO_6 is greatly decreased but not eliminated by this repeated annealing. The rounded CBTO particle size ranges from 100 nm to 10 μm in the powders annealed 4 times in the Cu-rich atmosphere.

4b. Optical and electronic properties

The wavelength-dependent optical absorption of the powders annealed 4 times in Cu-rich atmosphere, dispersed in a solvent,
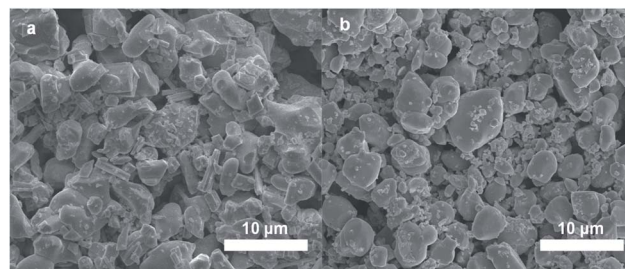

Fig. 4 Scanning Electron Microscopy (SEM) top-view images of powders synthesized by (a) 1 time and (b) 4 times annealing in Cu-rich atmosphere.
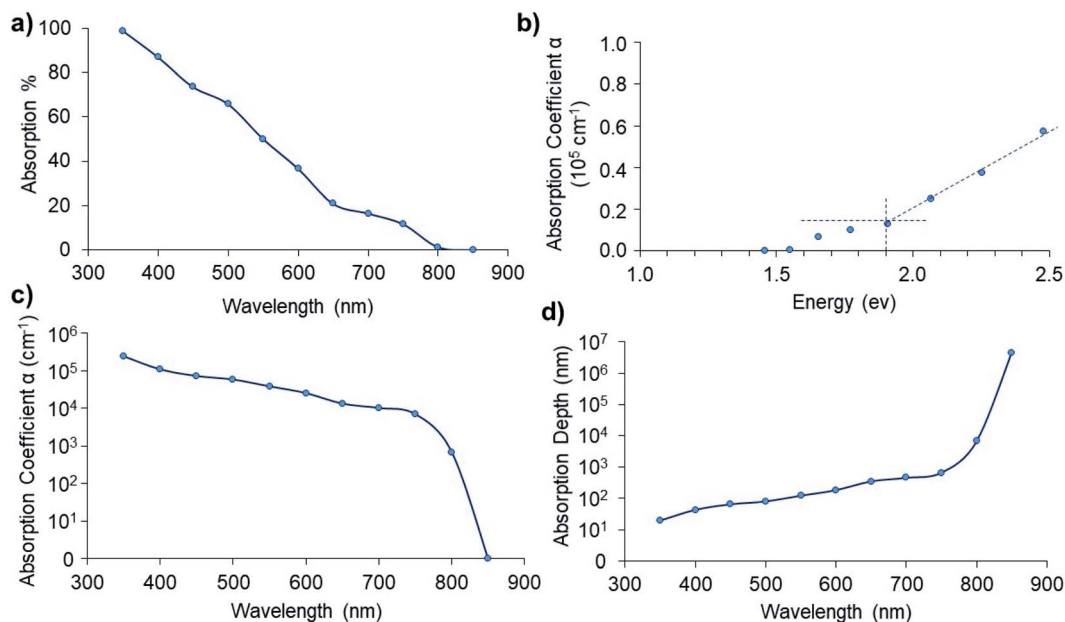
This journal is © The Royal Society of Chemistry 2021

J. Mater. Chem. A, 2021, **9**, 1643–1654 | **1647**

Fig. 5 Optical absorption of powders annealed 4 times in Cu-rich atmosphere. (a) Absorption (%) *vs.* wavelength, (b) absorption coefficient *vs.* energy, (c) absorption coefficient (log scale) *vs.* wavelength, and (d) absorption depth (log scale) *vs.* wavelength.

and drop-casted onto quartz substrates was measured using an integrating sphere with white-light illumination from a Xe lamp. The percentage of absorbed light was calculated from the measured reflection (R) and transmission (T) as absorption % = $[(1 - R - T)/(1 - R)] \times 100\%$, and is plotted *vs.* photon wavelength in Fig. 5a. It is seen from this plot that the material absorbs some light at wavelengths in the 650–800 nm range but has a sharper absorption onset at ~650 nm (~1.9 eV). The optical absorption coefficient (α) was calculated using the effective thickness (t) as $\alpha = -\ln(T/(1 - R))/t$. The effective thickness of the sample was 200 nm, which was calculated from the measured powder mass (m), sample area (A) and CBTO

density (ρ) as $t = m/(\rho A)$. The optical absorption coefficient is plotted *vs.* photon energy in Fig. 5b. This plot shows an absorption onset at ~1.9 eV (~650 nm), in addition to an absorption tail at lower energies (1.4–1.9 eV). A Tauc plot $((\alpha E)^{1/r}$ *vs. E*), where E is the photon energy, with exponent $r = 0.5$ has also been included in ESI Fig. S10,† which provides evidence for a direct band gap of ~1.95 eV. In addition, a direct band gap energy of ~1.97 eV is later provided by PL measurements, as well. Therefore, we conclude that CBTO has a direct band gap energy of ~1.9–2.0 eV. Fig. 5b is also directly comparable to the plot of the theoretically predicted absorption coefficient of CBTO containing Cu vacancies in Fig. 6b and is extremely
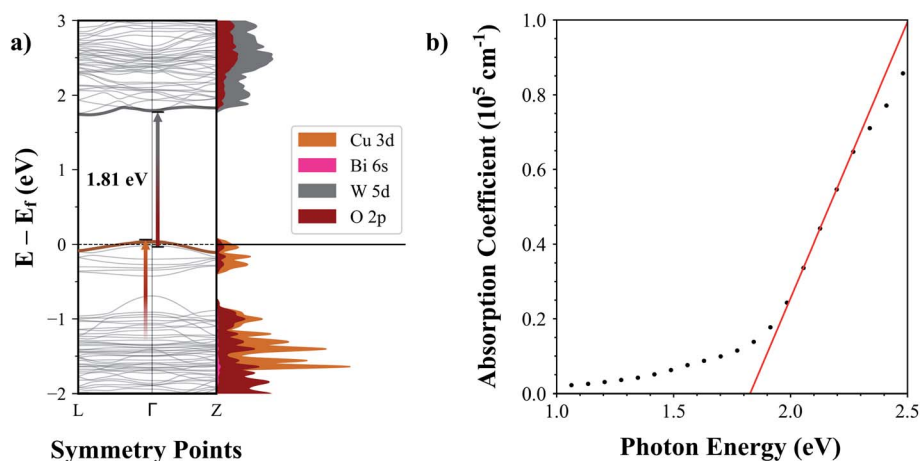

Fig. 6 (a) Calculated band structure and (b) calculated optical absorption for CBTO with Cu vacancy. The optical gap is calculated at 1.81 eV (upper arrow in a). The partially occupied band at the valence band maximum (shown in brown in a) is due to the energetically favorable Cu vacancy and consists primarily of Cu 3d states. This vacancy is expected to cause both p-type behavior of CBTO, as well as significant below-gap optical absorption (lower arrow in a and seen as an absorption tail in b).

1648 | *J. Mater. Chem. A*, 2021, **9**, 1643–1654

This journal is © The Royal Society of Chemistry 2021

similar. In both cases, there is a significant below-gap absorption tail, which is explained later by the theoretical result as being due to intra-valence band absorption associated with the Cu vacancy. In addition, some of this below-gap absorption tail may be due to absorption by the surface CuO impurity that was detected by XPS and PL, but not by XRD. The absorption coefficient of CuO is 10^4 to 10^5 cm^{-1} in the 1.5–2.0 eV range.[45] Even assuming a CuO absorption coefficient of 10^5 cm^{-1}, however, the total absorption by CuO cannot be more than ∼2% since the total fraction of the CuO impurity in this 200 nm-thick film is less than ∼1% based on the detection limit of XRD. However, the absorption by the sample at the CBTO band edge (650 nm) is ∼20%, meaning that the vast majority of the absorption, including the absorption tail in the 650–800 nm wavelength range, comes from the CBTO itself, which is consistent with the theoretical prediction. The absorption coefficient (α) and the absorption depth ($1/\alpha$) are plotted in Fig. 5c and d, respectively. According to Fig. 5c, the absorption coefficient of CBTO is 10^4 to 10^5 cm^{-1} across the range of visible light. This is one order of magnitude higher than that of Si and similar to that of GaAs, CdTe, and BiVO$_4$.[46] Furthermore, as shown in Fig. 5d, most of the light with wavelength shorter than 600 nm can be absorbed within ∼200 nm thick CBTO.

Theoretical calculations of the band structure and optical absorption coefficient[47] were carried out in VASP[48] for a CBTO supercell with a single Cu vacancy, as such a defect was found to be the most probable one in Fig. 3. Details are provided in ESI† and results are given in Fig. 6. The calculated band structure (Fig. 6a) predicts that the main optical gap is due to the interband transition from the highest occupied O 2p state in the valence band to the W 5d conduction band minimum, and is calculated at 1.81 eV, which is consistent with the band gap obtained from the calculated absorption coefficient *vs.* photon energy (Fig. 6b). This is slightly smaller than the measured value of ∼1.9–2.0 eV but within the range expected, given the approximations and limitations of the theoretical methods used. The calculated band structure also reveals a partially filled band at the top of the valence band (shown in brown) reflecting the Cu vacancy, which is expected to render p-type character to

CBTO. In addition, the presence of this band results in significant below-gap absorption due to O 2p to Cu 3d intraband transitions from the occupied lower-lying valence band states to the band associated with the Cu vacancy. This results in the below-gap absorption tail in Fig. 6b, which is very similar to the tail seen experimentally in Fig. 5b. Our DFT calculations also predict a hole effective mass of 1.74 m_0 for hole transport in the Cu vacancy band, where m_0 is the rest mass of the electron. For comparison, our DFT calculations predict a hole effective mass of 1.13 m_0 for the Cu vacancy band of Cu$_2$O, a common p-type oxide, using the same level of theory. Hence based only on DFT effective mass calculations, CBTO would be expected to have a lower p-type band mobility than that of Cu$_2$O.

To determine the possible influence of Bi$_2$WO$_6$ impurity on the electronic properties, we calculated the band offset between CBTO and Bi$_2$WO$_6$. The band offset plot and its details are given in ESI (Fig. S11†). Results show that CBTO and Bi$_2$WO$_6$ form a type II band offset, with lower band edges at Bi$_2$WO$_6$. According to our calculations, the top of the valence band of CBTO is ∼1.3 eV higher than that of Bi$_2$WO$_6$, and the bottom of the conduction band is ∼0.7 eV higher than that of Bi$_2$WO$_6$. Hence, we can conclude that Bi$_2$WO$_6$ impurity may serve as an electron trap in CBTO.

The time-integrated PL spectrum of 4 times Cu-rich annealed powders drop-casted on quartz substrate excited by the 485 nm line of a 10 Hz, 4 ns pulsed Nd:YAG laser is shown in Fig. 7a. The sample exhibits a strong PL peak at 630 nm (1.97 eV), which we ascribe to the direct band gap of CBTO, and a weak and broad PL peak at 880 nm (1.41 eV). This result indicates that the CBTO has a direct band gap of 1.97 eV, which matches the result of our light absorption measurement (direct band gap of ∼1.9–2.0 eV), while the broad PL peak at 880 nm is likely from a surface impurity phase of CuO (band gap 1.35 eV–1.60 eV)[49] that was detected by XPS measurement.

The radiative lifetime of photoexcited carriers in CBTO was characterized by time-resolved photoluminescence (TRPL). TRPL measurement was performed at room temperature with 633 nm excitation pulses produced by an Nd:YAG laser with 20 ps pulse duration and 19.4 MHz repetition rate. The emission
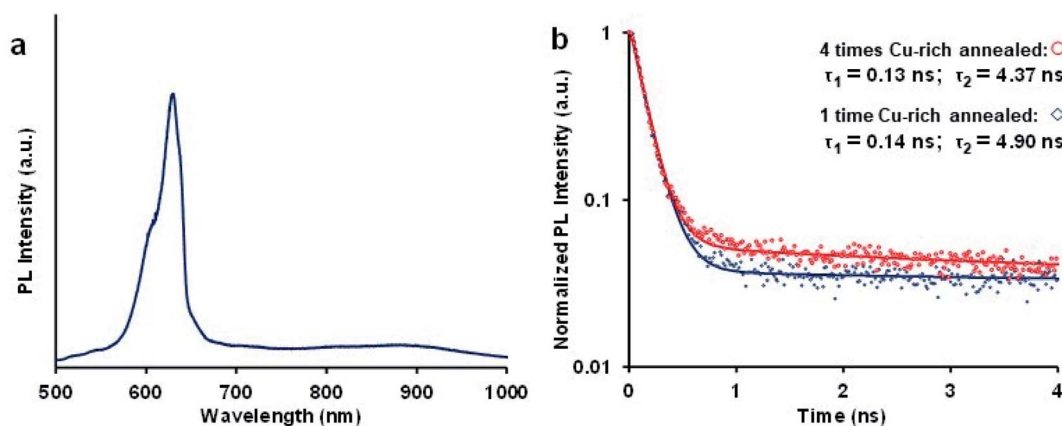

Fig. 7 (a) Photoluminescence (PL) spectrum of powders annealed 4 times in Cu-rich atmosphere. (b) Time-resolved PL (TRPL) decay measurements of emission from powders annealed 4 times (red) and 1 time (blue) in Cu-rich atmosphere from 530 nm to 750 nm.

was collected using a time correlated single photon counting system (Becker & Hickl SPC-150) and the signal was integrated using a single photon avalanche photodiode (ID Quantique ID-100-50-std). The time-averaged pulsed laser power (P_{avg}) was measured by a calibrated silicon photodiode to be 0.5 μW, and the illuminated area of the sample was 1 mm^2. The instantaneous pulsed laser intensity (I_{inst}, i.e. the intensity of the laser when it is on) is calculated from P_{avg}, the pulse duration (t_{on}), repetition frequency (F) and illuminated area (A) as $I_{inst} = P_{avg}/(t_{on} \times F \times A)$, and is equal to ~130 mW cm^{-2}. Since the absorption depth for 633 nm excitation is less than 0.5 μm in CBTO (as shown in Fig. 5d) and the pellet is 450 μm thick, we can assume that most of this light is absorbed. The photon flux from the laser corresponding to this intensity is ~4 × 10^{21} m^{-2} s^{-1}, which is of a similar magnitude as the photon flux that would be absorbed by CBTO under one sun illumination up to its band gap wavelength (~1 × 10^{21} m^{-2} s^{-1}). Thus, the photoexcited carrier radiative lifetime obtained from this TRPL measurement is similar to the lifetime that can be expected under one-sun illumination conditions. Pellets formed from 1-time Cu-rich annealed powders and 4-times Cu-rich annealed powders were used for the TRPL measurements, and the results are plotted in Fig. 7b. The TRPL decay dynamics of the emissions from the 1-time Cu-rich annealed and 4-times Cu-rich annealed samples in the direct band gap region (530 nm to 750 nm) were accurately fitted by double exponential decays with time constants of 0.13 ns and 4.37 ns, and 0.14 ns and 4.90 ns, respectively. The contribution of the decay signals from the longer decay time in both of cases are neglected because they are ascribed to internal light reflection within the TRPL system, and the 0.13 ns and 0.14 ns decay time are taken to be the direct bandgap photoexcited carrier lifetime in 1-time Cu-rich annealed and 4-times Cu-rich annealed samples, respectively. Based on this result, the decrease of the Bi_2WO_6 impurity in the 4-times Cu-rich annealed sample compared to the 1-time Cu-rich annealed sample does not appear to influence the radiative lifetime of photoexcited carriers.

The electrical transport properties of CBTO were characterized by Hall effect measurement (MMR Technologies K2500) using van der Pauw method in a magnetic field of 12 500 G, with a current of 36.7 nA. The CBTO sample for Hall effect measurement was prepared by thermal evaporation of 70 nm-thick gold contacts onto the four corners of a square-shaped 4-times Cu-rich annealed pellet. The pellet has a lateral size of 1 cm × 1 cm with thickness of 450 μm, while the gold contacts at the corners each had a size of ~ 1 mm × 1 mm and had 7.5 mm center-to-center spacing. The majority carrier type of the pellet was found to be holes (p-type semiconductor) with carrier density of 3.0 × 10^{13} cm^{-3}. The p-type doping in CBTO is typical of Cu-containing compounds due to Cu vacancies, as in Cu_2O,[50] Cu_2S,[51] and CZTS.[52] Carrier density depends on the formation energy of the source. As previously mentioned, our DFT calculations have determined the source of p-type carriers in CBTO to be spontaneously-forming Cu vacancies with formation energy of 0.35 eV. For another p-type oxide, namely Cu_2O, which also has p-type carriers due to Cu vacancies, Soon et al. calculated a Cu vacancy formation energy of 0.28 eV at the

DFT(PBE) theory level.[53] Nolan and Elliott calculated a value of 0.34 eV for a similar size supercell at the DFT+U ($U = 7$ eV) theory level.[50] Therefore, based only on these formation energies, we would expect CBTO and Cu_2O to have similar carrier densities. Experimentally, the carrier density in p-type Cu_2O has been measured to be as low as 10^{13} cm^{-3} in thin films,[54] and as low as 10^9 cm^{-3} in single crystals.[55] Therefore, the 3 × 10^{13} cm^{-3} carrier density determined here for CBTO is comparable to the values obtained for the similar binary oxide, Cu_2O. Furthermore, the Cu-rich synthesis conditions employed here may also be responsible for suppressing the formation of Cu vacancies in CBTO and resulting in a low carrier concentration.

The Hall effect measurement also yields a long-range charge carrier mobility of 0.32 cm^2 V^{-1} s^{-1}. The low Hall mobility is indicative of the deleterious effect of grain boundaries and defect-associated trap states and suggest that long-range transport occurs by hopping and de-trapping. Nonetheless, this mobility is still one order of magnitude larger than that in $BiVO_4$ and two orders of magnitude larger than that in $CuBi_2O_4$. Combined with the carrier lifetime of 0.13 ns as determined from TRPL measurements, this mobility results in a photoexcited carrier diffusion length (L) of $L = (\tau \mu KT/e)^{0.5} \sim 10.3$ nm, where τ is the carrier lifetime, μ is Hall carrier mobility, K is Boltzmann's constant, T is absolute temperature and e is the electron charge. This diffusion length is comparable to that in the successful oxides $BiVO_4$ (~70 nm) and $CuBi_2O_4$ (~50 nm), for instance.[23,56] However, the optical absorption depth of 100–200 nm is larger than the carrier diffusion length, meaning that heterojunction device architectures involving the coating of thin CBTO layers onto nanostructured charge transport layers or current collectors may be necessary for achieving high-efficiency solar energy conversion.

We then performed UPS measurements of the 4-times Cu-rich annealed pellet in order to determine the band energies and Fermi level of CBTO. These measurements are crucial for the selection of n-type heterojunction partners with appropriate band energies for pairing with CBTO. The UP spectrum (ESI Fig. S12†) was measured at a sample bias ($V_b = -5$ V). The work-function of a semiconductor surface (ϕ_s) is given by $\phi_s = h\nu - E_{SE} - V_b$, where $h\nu$ represents the energy of the photons used to probe the band-structure (21.2 eV in our case) and E_{SE} is the secondary electron cut-off energy. The work function was found to be 5.15 eV and the energy of the top of the valence band (VBM) was found to be −5.81 eV vs. vacuum (Fig. S12c†). This UPS result indicates that CBTO would make a good heterojunction with the widely used n-type metal oxide material ZnO.[57]

Future CBTO-based photovoltaic devices necessitate depositing CBTO on current collectors such as TCOs. We have evaluated thin films of interconnected CBTO particles on ITO and on quartz by SEM and XRD and studied the microscopic photoconductivity on interconnected CBTO films on quartz using OPTP spectroscopy. For this, 4-times Cu-rich annealed powders were drop-casted on quartz and ITO substrates followed by annealing in sealed Cu boxes in a tube furnace at 500 °C. This annealing temperature of 500 °C is lower than the 600 °C temperature used to anneal the powders initially. This temperature reduction is needed to minimize rapid diffusion of

1650 | J. Mater. Chem. A, 2021, 9, 1643–1654

This journal is © The Royal Society of Chemistry 2021

Cu into the ITO and glass substrate. At lower temperature, we observed no change in appearance of the ITO or quartz substrates and no changes in the XRD patterns (Fig. S13†). However, SEM (Fig. S14†) showed that the particle size and inter-connectedness of CBTO particles in the films increased after annealing due to sintering. Such changes are likely to improve electrical properties of CBTO films by forming pathways for long-range transport of carriers. To assess the effect of higher inter-particle connectivity in the annealed films composed of connected CBTO particles compared to un-annealed films composed of separated CBTO particles, we have studied transient microscopic THz photoconductivity in the two films on quartz substrates. Optical pump – THz probe spectroscopy (OPTP) is a contact-free technique sensitive to motion of photoexcited carriers on picoseconds time scales.[58–63] With THz photon energy in meV range, OPTP is particularly sensitive to free (mobile) carriers. Unlike the Hall effect that measures carrier transport over macroscopic distances between the electrical contacts, and can detect slow carrier transport that proceeds by hopping and carrier trapping and de-trapping, OPTP probes carrier transport over tens and hundreds of nanometers, thus allowing us to follow behavior of photoexcited free carriers within individual CBTO particles.

Annealed and unannealed CBTO films (consisting of inter-connected particles and separate particles, respectively) on quartz were excited by ~100 fs duration, 400 nm, 0.5 μJ cm^{-2} pulses from a regeneratively amplified 1 kHz repetition rate Ti : sapphire laser at normal incidence as described previously.[61,62] The sample was placed behind a 1.5 mm aperture in the center of a ~3 mm diameter beam spot to ensure uniform excitation of the studied portion of the film. THz probe pulses were generated using optical rectification of the 800 nm pulses from the same laser source in a 1 mm thick [110] ZnTe crystal and focused onto the sample by off-axis parabolic mirrors. Transmitted THz pulses were detected using electro-optic sampling in a second [110] ZnTe crystal. Fig. 8a shows the normalized change in transmission of the main peak of the THz probe pulse as a function of 400 nm pump-THz probe delay time. In the limit of low relative pump-induced change in transmission, $-\Delta T(t)$ is proportional to the transient pump-induced photoconductivity.[64–66]

We find that in both CBTO films, photoconductivity after an initial fast increase due to the photoexcitation, exhibits a bi-exponential decay with one decay time in the picoseconds, and another one in tens of picoseconds. The two decay times represent two different mechanisms of free carrier trapping. Both fast and slow decay components are faster in the un-annealed film, at 1 ps vs. 2 ps and 16 ps vs. 40 ps as free carriers are more likely to encounter grain boundary and bulk defects in smaller particles of the un-annealed film. The fast decay component is also less pronounced in the un-annealed CBTO film compared to the annealed one. As the major difference between the film is interconnectedness of the CBTO particles, fastest trapping time may be due to the inter-grain
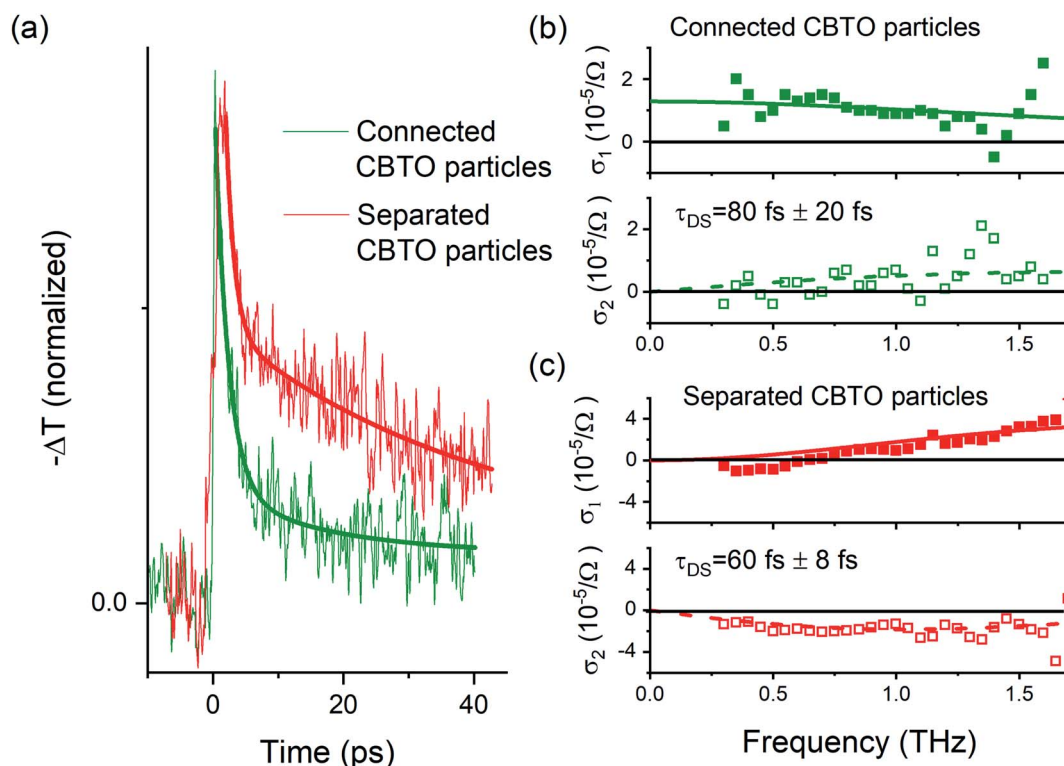

Fig. 8 Optical pump – THz probe spectroscopy. (a) Picosecond dynamics of photoconductivity in annealed (connected CBTO particles) and un-annealed (separated CBTO particles) films following photoexcitation with 400 nm, ~100 fs pulses. (b and c) Real (solid squares) and imaginary (open squares) photoconductivity for two the two films 2 ps after photoexcitation. The lines in (b and c) represent a global fit of real and imaginary components of the conductivity to the Drude−Smith model (eqn (1)).

This journal is © The Royal Society of Chemistry 2021

J. Mater. Chem. A, 2021, **9**, 1643–1654 | **1651**

trap states. Here it is important to underscore the difference between the lifetime of free carriers measured by OPTP spectroscopy and the much longer radiative lifetime measured by TRPL spectroscopy. During OPTP spectroscopy, photoexcitation initially creates free carriers that move with fast band-like transport in CBTO. Over the initial picoseconds to tens of picoseconds after optical excitation, THz pulses are absorbed by these free, band-like carriers. As these free carriers get trapped at defect states, they can still contribute to trapping and de-trapping as well as slow hopping transport that can be detected by the Hall effect measurement but not by OPTP spectroscopy. Eventually, the trapped photoexcited carriers recombine, and the radiative recombination lifetime determined by the TRPL spectroscopy (~0.1 ns) provides a good estimate of the overall lifetime of the photoexcited carriers provided that the non-radiative recombination is not a major contributor. As such, OPTP and TRPL spectroscopy provide complementary information and allow us to re-construct a more complete picture of photoexcited carrier dynamics: photoexcitation generates free, highly mobile carriers that become trapped in defect states over the initial tens of picoseconds; after that, slow hopping motion of carriers in shallow trap states continues contributing to the long-range conductivity with a mobility of $0.32 \text{ cm}^2 \text{ V}^{-1} \text{ s}^{-1}$.

To estimate initial mobility of the free carrier population soon after optical injection, we have also measured frequency-resolved complex photoconductivity in both CBTO film on quartz. The complex conductivity is extracted from photoexcitation-induced changes in the amplitude and the phase of the THz pulse waveform transmitted through the sample.[58,64,67,68] Real and imaginary conductivity spectra at 2 ps after excitation of the annealed and un-annealed films are shown in Fig. 8b and c, respectively. In general, behavior of free carriers in granular and nanostructures materials can be described by the Drude–Smith model, a phenomenological modification of the Drude model for free carrier conductivity, that accounts for the charge carrier confinement over mesoscopic length scales.[66,68–76] In the Drude–Smith model, the complex conductivity is given to the first order by

$$\sigma(\omega) = \frac{\sigma_0}{1 - i\omega\tau_{DS}}\left[1 + \frac{c}{1 - i\omega\tau_{DS}}\right] \qquad (1)$$

where σ_0 is the scaling factor dependent on carrier density and c-parameter characterizes the degree of carrier localization due to the presence of grain boundaries. For $c = 0$, this model reduces to the Drude model for free carriers and σ_0 becomes the long-range, DC conductivity, while $c = -1$ describes situations in which carriers are completely localized within individual grains, and the long-range, inter-granular conductivity is completely suppressed. The global fits of real and imaginary components of the photoconductivity to the Drude–Smith model are shown in Fig. 8b and c as lines. We find that annealing CBTO film on quartz that results in the increase in film connectivity observed in SEM leads to a dramatic improvement in long-range mobility of free carriers, as c-parameter goes from nearly −1 to 0. Another parameter in the Drude–Smith model, the effective scattering time τ_{DS} takes into account intrinsic electron-lattice scattering (τ_{int}), collisions with grain boundaries ($\tau_{boundary}$) and carrier–carrier scattering in the case of high excitation densities.[65,77] We find that τ_{DS} is ~80 fs in the annealed film, improved from ~60 fs in un-annealed film. Shorter scattering time in un-annealed film composed of separated CBTO particles likely reflects additional scattering from particle boundaries as well as bulk defects. Finally, we can use τ_{DS} to calculate free carrier mobility (limited to the intra-grain mobility in the case of the un-annealed film), and we find that it is ~150 $\text{cm}^2 \text{ v}^{-1} \text{ s}^{-1}$ for the annealed and ~110 $\text{cm}^2 \text{ v}^{-1} \text{ s}^{-1}$ for the un-annealed film. The free, band-like carriers in the annealed film have long-range the mobility $\mu_{long-range} = \frac{e}{m^*}\tau_{DS}(1 + c)$ that is almost three orders of magnitude larger than the measured Hall mobility, but very short lifetime of picoseconds. It was mentioned earlier that, based only on DFT effective mass calculations, CBTO with larger hole effective mass of 1.74 m_0 would be expected to have a lower p-type band mobility than that of Cu_2O with hole effective mass of 1.13 m_0. Typical hole mobilities for Cu_2O single crystals are of order 100 $\text{cm}^2 \text{ V}^{-1} \text{ s}^{-1}$,[78] although hole mobilities as high as 256 $\text{cm}^2 \text{ V}^{-1} \text{ s}^{-1}$ have been achieved in Cu_2O.[54] Therefore, the mobility value of ~150 $\text{cm}^2 \text{ V}^{-1} \text{ s}^{-1}$ for band-like transport of free p-type carriers in CBTO obtained here is reasonable. Finally, therefore, the band-like motion of free carriers with high mobility (150 $\text{cm}^2 \text{ v}^{-1} \text{ s}^{-1}$) and picosecond lifetime detected by OPTP, and the slow hopping motion of trapped carriers with low mobility (0.32 $\text{cm}^2 \text{ V}^{-1} \text{ s}^{-1}$) and nanosecond lifetime detected by Hall effect and TRPL result in comparable diffusion lengths. This result underscores that annealing films of CBTO particles indeed results in material in which both free carrier transport and hopping and trapping/de-trapping transport can be harnessed.

5. Conclusions

In conclusion, following a theoretical prediction, the quaternary metal oxide semiconductor CBTO was successfully synthesized by a Cu-rich solid-state synthesis method, in which Bi_2O_3, Cu_2O, WO_3 powders were mixed, annealed and reacted 4 times in a Cu-rich argon environment at 600 °C. The synthesis resulted in CBTO with Bi_2WO_6 bulk impurity and CuO surface impurity. The Bi_2WO_6 impurity increased with annealing temperature up to 800 °C, and theoretical predictions confirmed that it is expected to co-exist with CBTO at thermodynamic equilibrium. Powders, sintered pellets, and sintered thin films of the CBTO material were prepared, and the optical, electrical and photoelectrical properties were measured and studied for the first time. CBTO is found to have a direct band gap of ~1.9–2.0 eV and optical absorption coefficient of 10^4–10^5 cm^{-1} for visible photons, with a significant below-gap absorption tail that theoretical calculations show is due to intra-valence band absorption associated with Cu vacancies. These Cu vacancies are also responsible for the observed p-type conductivity, with measured carrier density of $3.0 \times 10^{13} \text{ cm}^{-3}$. Our theoretical calculations also show that CBTO and Bi_2WO_6 impurity have type II band offset, with Bi_2WO_6 impurity potentially contributing to electron trapping. Based on band alignment, CBTO

1652 | *J. Mater. Chem. A*, 2021, **9**, 1643–1654

This journal is © The Royal Society of Chemistry 2021

may form a favorable p–n junction with ZnO, which points to a direction for the realization of photovoltaics based on CBTO. Interestingly, both fast band-like transport of shorter-lived free carriers with 150 $cm^2 V^{-1} s^{-1}$ mobility and slow hopping transport of longer-lived trapped carriers with 0.32 $cm^2 V^{-1} s^{-1}$ mobility result in comparable diffusion lengths of ~10 nm in CBTO. However, this carrier diffusion length is shorter than the optical absorption depth (100–200 nm), which means that nanostructured heterojunctions with n-type materials such as ZnO will likely be needed to achieve efficient solar energy conversion.

Author contributions

L. Z. carried out the CBTO synthesis and the optical, SEM and XRD characterization of the CBTO. M. M. performed the XPS and UPS measurements (under the supervision of A. C. and R. L. G.), and also the PL measurements. B. G. performed the Hall effect measurements. G. L. and L. V. T. performed the THz spectroscopy measurements. E. B. and M. N. H. performed the theoretical calculations. L. Z., E. B., M. N. H., L. V. T. and P. M. R conceived the study and wrote the manuscript. All authors discussed the results and commented on the manuscript.

Conflicts of interest

There are no conflicts of interest to declare.

Acknowledgements

References

1 F. Shimura, in *Springer Handbook of Electronic and Photonic Materials*, ed. S. Kasap and P. Capper, Springer International Publishing, Cham, 2017, pp. 1–1, DOI: 10.1007/978-3-319-48933-9_13.

2 Y. Liu, H. K. Turley, J. R. Tumbleston, E. T. Samulski and R. Lopez, *Appl. Phys. Lett.*, 2011, **98**(16), 162105.

3 T. Minami, J. Yamazaki and T. Miyata, *MRS Commun.*, 2016, **6**, 416–420.

4 M. Tadatsugu, N. Yuki and M. Toshihiro, *Appl. Phys. Express*, 2013, **6**, 044101.

5 L. Zhou, Y. Yang, J. Zhang and P. M. Rao, *ACS Appl. Mater. Interfaces*, 2017, **9**, 11356–11362.

6 L. Zhou, C. Zhao, B. Giri, P. Allen, X. Xu, H. Joshi, Y. Fan, L. V. Titova and P. M. Rao, *Nano Lett.*, 2016, **16**, 3463–3474.

7 T. W. Kim and K.-S. Choi, *Science*, 2014, **343**(6174), 990–994.

8 V. Srikant and D. R. Clarke, *J. Appl. Phys.*, 1998, **83**, 5447–5451.

9 M. Caglar, S. Ilican, Y. Caglar and F. Yakuphanoglu, *Appl. Surf. Sci.*, 2009, **255**, 4491–4496.

10 Y. Toshinari, M. Uichiro and I. Yoshiro, *Jpn. J. Appl. Phys.*, 1983, **22**, 454.

11 F. J. Arlinghaus, *J. Phys. Chem. Solids*, 1974, **35**, 931–935.

12 P. P. González-Borrero, F. Sato, A. N. Medina, M. L. Baesso, A. C. Bento, G. Baldissera, C. Persson, G. A. Niklasson, C. G. Granqvist and A. F. d. Silva, *Appl. Phys. Lett.*, 2010, **96**, 061909.

13 F. Wang, C. Di Valentin and G. Pacchioni, *J. Phys. Chem. C*, 2011, **115**, 8345–8353.

14 W. D. Chemelewski, O. Mabayoje, D. Tang, A. J. E. Rettie and C. Buddie Mullins, *Phys. Chem. Chem. Phys.*, 2016, **18**, 1644–1648.

15 B. M. Warnes, F. F. Aplan and G. Simkovich, *Solid State Ionics*, 1984, **12**, 271–276.

16 L. Qiao, H. Y. Xiao, H. M. Meyer, J. N. Sun, C. M. Rouleau, A. A. Puretzky, D. B. Geohegan, I. N. Ivanov, M. Yoon, W. J. Weber and M. D. Biegalski, *J. Mater. Chem. C*, 2013, **1**, 4628–4633.

17 M. Rohloff, B. Anke, S. Zhang, U. Gernert, C. Scheu, M. Lerch and A. Fischer, *Sustainable Energy Fuels*, 2017, **1**, 1830–1846.

18 T. W. Kim, Y. Ping, G. A. Galli and K.-S. Choi, *Nat. Commun.*, 2015, **6**, 8769.

19 F. Biccari, C. Malerba and A. Mittiga, *Sol. Energy Mater. Sol. Cells*, 2010, **94**, 1947–1952.

20 M. Nolan and S. D. Elliott, *Chem. Mater.*, 2008, **20**, 5522–5531.

21 E. Bainglass and M. N. Huda, *J. Electrochem. Soc.*, 2019, **166**, H3195–H3201.

22 J. H. Kim, J.-W. Jang, Y. H. Jo, F. F. Abdi, Y. H. Lee, R. van de Krol and J. S. Lee, *Nat. Commun.*, 2016, **7**, 13380.

23 F. F. Abdi, T. J. Savenije, M. M. May, B. Dam and R. van de Krol, *J. Phys. Chem. Lett.*, 2013, **4**, 2752–2757.

24 D. Cao, N. Nasori, Z. Wang, Y. Mi, L. Wen, Y. Yang, S. Qu, Z. Wang and Y. Lei, *J. Mater. Chem. A*, 2016, **4**, 8995–9001.

25 S. O. Alfaro and A. Martínez-de la Cruz, *Appl. Catal., A*, 2010, **383**, 128–133.

26 L. Jing, S. Qingzhu, C. Yan and S. Ming, *IOP Conf. Ser.: Earth Environ. Sci.*, 2017, **100**, 012030.

27 G. Sharma, Z. Zhao, P. Sarker, B. A. Nail, J. Wang, M. N. Huda and F. E. Osterloh, *J. Mater. Chem. A*, 2016, **4**, 2936–2942.

28 S. P. Berglund, F. F. Abdi, P. Bogdanoff, A. Chemseddine, D. Friedrich and R. van de Krol, *Chem. Mater.*, 2016, **28**, 4231–4242.

29 X. Zhu, Z. Guan, P. Wang, Q. Zhang, Y. Dai and B. Huang, *Chin. J. Catal.*, 2018, **39**, 1704–1710.

30 F. Wang, W. Septina, A. Chemseddine, F. F. Abdi, D. Friedrich, P. Bogdanoff, R. van de Krol, S. D. Tilley and S. P. Berglund, *J. Am. Chem. Soc.*, 2017, **139**, 15094–15103.

31 J. Li, M. Griep, Y. Choi and D. Chu, *Chem. Commun.*, 2018, **54**, 3331–3334.

32 P. Sarker, D. Prasher, N. Gaillard and M. N. Huda, *J. Appl. Phys.*, 2013, **114**, 133508.

33 Y.-j. Liu, R. Cai, T. Fang, J.-g. Wu and A. Wei, *Mater. Res. Bull.*, 2015, **66**, 96–100.

34 S. J. Lee, Y. Kim, J.-Y. Hwang, J.-H. Lee, S. Jung, H. Park, S. Cho, S. Nahm, W. S. Yang, H. Kim and S. H. Han, *Sci. Rep.*, 2017, **7**, 3131.

35 T. F. Krüger and H. Müller-Buschbaum, *J. Alloys Compd.*, 1992, **190**, L1–L3.

36 F. Tolun and S. Celik, *Mater. Test.*, 2016, **58**, 735–741.

37 P. Sarker, M. M. Al-Jassim and M. N. Huda, *J. Appl. Phys.*, 2015, **117**, 035702.

38 P. Hohenberg and W. Kohn, *Phys. Rev.*, 1964, **136**, B864–B871.

39 G. Panzner, B. Egert and H. P. Schmidt, *Surf. Sci.*, 1985, **151**, 400–408.

40 M. A. Rafea and N. Roushdy, *J. Phys. D: Appl. Phys.*, 2008, **42**, 015413.

41 S. Choudhary, J. V. N. Sarma, S. Pande, S. Ababou-Girard, P. Turban, B. Lepine and S. Gangopadhyay, *AIP Adv.*, 2018, **8**, 055114.

42 T. Minami, Y. Nishi, T. Miyata and J.-i. Nomoto, *Appl. Phys. Express*, 2011, **4**, 062301.

43 W. Wang, M. Guo, D. Lu, W. Weimin and H. Wang, *Effect of HNO₃ Concentration on the Morphologies and Properties of Bi₂WO₆ Photocatalyst Synthesized by a Hydrothermal Method*, 2016.

44 Z. Sun, J. Guo, S. Zhu, L. Mao, J. Ma and D. Zhang, *Nanoscale*, 2014, **6**, 2186–2193.

45 C. Guillén and J. Herrero, *J. Alloys Compd.*, 2018, **737**, 718–724.

46 F. Deng, H. Cao, L. Liang, J. Li, J. Gao, H. Zhang, R. Qin and C. Liu, *Opt. Lett.*, 2015, **40**, 1282–1285.

47 H. Akkus and A. M. Mamedov, *J. Phys.: Condens. Matter*, 2007, **19**, 116207.

48 M. Gajdoš, K. Hummer, G. Kresse, J. Furthmüller and F. Bechstedt, *Phys. Rev. B: Condens. Matter Mater. Phys.*, 2006, **73**, 045112.

49 V. Jeyalakshmi, R. Mahalakshmy, K. Kr and B. Viswanathan, *Mater. Sci. Forum*, 2012, **734**, 1–62.

50 M. Nolan and S. D. Elliott, *Phys. Chem. Chem. Phys.*, 2006, **8**, 5350–5358.

51 A. Nayak, T. Ohno, T. Tsuruoka, K. Terabe, T. Hasegawa, J. K. Gimzewski and M. Aono, *Adv. Funct. Mater.*, 2012, **22**, 3606–3613.

52 D. Han, Y. Y. Sun, J. Bang, Y. Y. Zhang, H.-B. Sun, X.-B. Li and S. B. Zhang, *Phys. Rev. B: Condens. Matter Mater. Phys.*, 2013, **87**, 155206.

53 A. Soon, X.-Y. Cui, B. Delley, S.-H. Wei and C. Stampfl, *Phys. Rev. B: Condens. Matter Mater. Phys.*, 2009, **79**, 035205.

54 B. S. Li, K. Akimoto and A. Shen, *J. Cryst. Growth*, 2009, **311**, 1102–1105.

55 K. Matsuzaki, K. Nomura, H. Yanagi, T. Kamiya, M. Hirano and H. Hosono, *Appl. Phys. Lett.*, 2008, **93**, 202107.

56 S. Giménez and J. Bisquert, *Photoelectrochemical solar fuel production: From basic principles to advanced devices*, 2016.

57 S. S. Wilson, J. P. Bosco, Y. Tolstova, D. O. Scanlon, G. W. Watson and H. A. Atwater, *Energy Environ. Sci.*, 2014, **7**, 3606–3610.

58 P. U. Jepsen, D. G. Cooke and M. Koch, *Laser Photonics Rev.*, 2011, **5**, 124–166.

59 J. B. Baxter, C. Richter and C. A. Schmuttenmaer, *Annu. Rev. Phys. Chem.*, 2014, **65**, 423–447.

60 K. P. Regan, C. Koenigsmann, S. W. Sheehan, S. J. Konezny and C. A. Schmuttenmaer, *J. Phys. Chem. C*, 2016, **120**, 14926–14933.

61 K. T. Butler, B. J. Dringoli, L. Zhou, P. M. Rao, A. Walsh and L. V. Titova, *J. Mater. Chem. A*, 2016, **4**, 18516–18523.

62 K. Kushnir, K. Chen, L. Zhou, B. Giri, R. L. Grimm, P. M. Rao and L. V. Titova, *J. Phys. Chem. C*, 2018, **122**, 11682–11688.

63 L. V. Titova, T. L. Cocker, D. G. Cooke, X. Wang, A. Meldrum and F. A. Hegmann, *Phys. Rev. B*, 2011, **83**.

64 F. A. Hegmann, O. Ostroverkhova and D. G. Cooke, in *Photophysics of Molecular Materials*, Wiley-VCH Verlag GmbH & Co. KGaA, 2006, ch. 7, pp. 367–428, DOI: 10.1002/3527607323.

65 L. V. Titova, T. L. Cocker, D. G. Cooke, X. Wang, A. Meldrum and F. A. Hegmann, *Phys. Rev. B*, 2011, **83**, 085403.

66 C. A. Schmuttenmaer, *Chem. Rev.*, 2004, **104**, 1759–1780.

67 J. B. Baxter and G. W. Guglietta, *Anal. Chem.*, 2011, **83**, 4342–4368.

68 J. B. Baxter and C. A. Schmuttenmaer, *J. Phys. Chem. B*, 2006, **110**, 25229–25239.

69 N. Smith, *Phys. Rev. B*, 2001, **64**.

70 Z. Mics, A. D'Angio, S. A. Jensen, M. Bonn and D. Turchinovich, *Appl. Phys. Lett.*, 2013, **102**, 231120.

71 J. R. Knab, X. Lu, F. A. Vallejo, G. Kumar, T. E. Murphy and L. M. Hayden, *Opt. Mater. Express*, 2014, **4**, 300–307.

72 T. L. Cocker, D. Baillie, M. Buruma, L. V. Titova, R. D. Sydora, F. Marsiglio and F. A. Hegmann, *Phys. Rev. B*, 2017, **96**, 205439.

73 P. Parkinson, J. Lloyd-Hughes, Q. Gao, H. H. Tan, C. Jagadish, M. B. Johnston and L. M. Herz, *Nano Lett.*, 2007, **7**, 2162–2165.

74 D. G. Cooke, A. Meldrum and P. Uhd Jepsen, *Appl. Phys. Lett.*, 2012, **101**, 211107.

75 Q.-l. Zhou, Y. Shi, B. Jin and C. Zhang, *Appl. Phys. Lett.*, 2008, **93**, 102103.

76 B. G. Alberding, P. A. DeSario, C. R. So, A. D. Dunkelberger, D. R. Rolison, J. C. Owrutsky and E. J. Heilweil, *J. Phys. Chem. C*, 2017, **121**, 4037–4044.

77 G. M. Turner, M. C. Beard and C. A. Schmuttenmaer, *J. Phys. Chem. B*, 2002, **106**, 11716–11719.

78 S. T. Omelchenko, Y. Tolstova, S. S. Wilson, H. A. Atwater and N. S. Lewis, *2015 IEEE 42nd Photovoltaic Specialist Conference*, PVSC, 2015, pp. 1–4, DOI: 10.1109/PVSC.2015.7355920.